PCCP

Accepted Manuscript

This is an *Accepted Manuscript*, which has been through the Royal Society of Chemistry peer review process and has been accepted for publication.

Accepted Manuscripts are published online shortly after acceptance, before technical editing, formatting and proof reading. Using this free service, authors can make their results available to the community, in citable form, before we publish the edited article. We will replace this *Accepted Manuscript* with the edited and formatted *Advance Article* as soon as it is available.

You can find more information about *Accepted Manuscripts* in the **Information for Authors**.

Please note that technical editing may introduce minor changes to the text and/or graphics, which may alter content. The journal's standard **Terms & Conditions** and the **Ethical guidelines** still apply. In no event shall the Royal Society of Chemistry be held responsible for any errors or omissions in this *Accepted Manuscript* or any consequences arising from the use of any information it contains.

ARTICLE

First-charge instabilities of layered-layered lithium-ion-battery materials

Jason R. Croy[a], Hakim Iddir[a]†, Kevin Gallagher[a], Christopher S. Johnson[a], Roy Benedek[a], and Mahalingam Balasubramanian[a]†

Li- and Mn-rich layered oxideswith composition $x\text{Li}_2\text{MnO}_3\bullet(1-x)\text{Li}M\text{O}_2$ enable high capacity and energy density Li-ion batteries, but suffer from degradation with cycling. Evidence of atomic instabilities during the first charge are addressed in this work with X-ray absorption spectroscopy, first principles simulation at the GGA+U level, and existing literature. The pristine material of composition $x\text{Li}_2\text{MnO}_3\bullet(1-x)\text{LiMn}_{0.5}\text{Ni}_{0.5}\text{O}_2$ is assumed in the simulations to have the form of LiMn_2 stripes, alternating with NiMn stripes, in the metal layers. The charged state is simulated by removing Li from the Li layer, relaxing the resultant system by steepest descents, then allowing the structure to evolve by molecular dynamics at 1000 K, and finally relaxing the evolved system by steepest descents. The simulations show that about ¼ of the oxygen ions in the Li_2MnO_3 domains are displaced from their original lattice sites, and form oxygen-oxygen bonds, which significantly lowers the energy, relative to that of the starting structure in which the oxygen sublattice is intact. An important consequence of the displacement of the oxygen is that it enables about ⅓ of the (Li_2MnO_3 domain) Mn ions to migrate to the delithiated Li layers. The decrease in the coordination of the Mn ions is about twice that of the Ni ions. The approximate agreement of simulated coordination number deficits for Mn and Ni following the first charge with analysis of EXAFS measurements on $0.3\text{Li}_2\text{MnO}_3\bullet0.7\text{LiMn}_{0.5}\text{Ni}_{0.5}\text{O}_2$ suggests that the simulation captures significant features of the real material.

I. Introduction

The enormous interest in the lithium-ion battery cathode materials $x\text{Li}_2\text{MnO}_3\bullet(1-x)\text{Li}M\text{O}_2$,[1] often referred to as Li and Mn rich layered oxides, may be gauged by the number of related publications, perhaps a thousand or more. These materials are distinguished by the ability to cycle a larger fraction of Li ions than other cathode materials (as well as the high specific density of Li in the Li_2MnO_3 component), and therefore offer the promise of extraordinarily high capacities and energy densities. Full commercial exploitation of these materials, however, has been delayed by the discovery of a slow degradation of the voltage with cycling.[2-4]

Nucleation and growth of an additional phase during cycling is widely thought to be responsible for the degradation. Candidates for the putative new phase are a spinel[5-7] or a defect spinel, but its presence in the bulk is not fully corroborated across multiple techniques, and does not satisfactorily explain the electrochemical behavior of these systems, especially during early cycles. Also, a detailed transformation mechanism of the layered structure of Li and Mn rich layered oxides to spinel[8] is yet to be demonstrated. Therefore, no consensus exists on the mechanisms of the structural transformation and the identity of the transformed phase. Furthermore, charge compensation processes, beyond traditional TM redox, and structural dynamics associated with the hysteresis phenomenon are not well understood. Experiment has suggested that Mn migration is a key factor in voltage fade and hysteresis,[9-11] and that a comprehensive electrochemical model should account for both. Owing to the many levels of complexity, a full understanding of these processes appears a distant prospect at this time.

Our focus in this article is restricted to the atomic instabilities that develop in the Li and Mn rich layered oxides during the first charge. Only with a better understanding of first charge processes are the subsequent phenomena of cycling likely to be unraveled. Evidence is evaluated from experiment, simulation, or a combination of the two. In particular, we present evidence that extension of the first charge of LL Li and Mn rich layered oxides into the plateau region (activation) results in (i) oxygen vacancies, (ii) Mn under-coordination, (iii) Mn migration, and (iv) interstitial oxygen. X-ray absorption experiments as well as first principles simulations on Li and Mn rich layered oxides are described. An interpretation in terms of the stabilizing effect of oxygen rebonding to form molecules in the massively hole-doped (electron-deficient) materials is given.

II. Experiment

X-ray absorption measurements are presented for $0.3\text{Li}_2\text{MnO}_3\bullet0.7\text{LiMn}_{0.5}\text{Ni}_{0.5}\text{O}_2$ (LMNO), synthesized via traditional transition-metal-hydroxide precursors as reported in (Johnson et al., 2004).[12] The LMNO powder was assembled in pouch cells for in-situ experiments as previously described.[10]

X-ray absorption near edge structure (XANES) and extended X-ray absorption fine structure (EXAFS) data were collected in transmission mode at the Sector 20 BM beamline of Argonne's Advanced Photon Source. Measurements of Mn and Ni K-edge

[a]. Argonne National Laboratory, Argonne, IL 60439.
† Corresponding authors

COMMUNICATION

spectra were made *in situ* at frequent time intervals during the first charge. The incident beam was monochromatized using a Si(111) fixed-exit, double-crystal monochromator. Manganese and nickel foils, as appropriate, were incorporated for energy calibration with the zero energy (E_0) defined according to Kraft et al.[13] Extraction of XANES/EXAFS data was performed by established methods using the ATHENA software package.[14, 15] Structural parameter fits were obtained with the ARTEMIS software package, which utilizes the IFEFFIT library of XAFS algorithms.[14, 15]

The electrochemistry of LMNO has been well studied and previously reported.[2, 12, 16] LMNO shows local Li_2MnO_3-like ordering, undergoes structural transformation and voltage fade, and exhibits the characteristic hysteresis. Hysteresis and voltage fade appear to be inherent, bulk properties of materials with Li- and Mn-rich Li_2MnO_3-like domains.[3] Thus, LMNO can be viewed as representative of this class of electrodes.

The nickel K-edge, LMNO XANES (not shown) agrees well with expected results[10, 17] and we focus herein on the unique features presented by the Mn K-edge. Figures 1 and 2 show in-situ Mn K-edge XANES data for LMNO. The electrode delivered a capacity of ~280 mAh/g at 4.9 V. Assuming full delithiation of the $LiMO_2$ component ($M = Mn_{0.5}Ni_{0.5}$), this capacity would correspond to ~50-60% activation of the Li_2MnO_3 component, which is likely a lower bound. The results shown in Figs. 1 and 2 are consistent with previous Mn K-edge absorption measurements for LMNO electrodes.[17-19] The edge and pre-edge features (line shapes, intensities and peak energies) evolve with increasing delithiation. The pre-edge peaks in Fig. 2 grow in intensity, likely due to increased structural disorder, however the resolution between peaks 1 and 2 diminishes and peak 2 shifts to lower energy while peak 1 remains largely unshifted, indicating the possibility of a new process contributing some intensity between the two. This behavior is in contrast to layered materials where significant Li and Mn order does not occur (e.g., NMC-111) in which cases the resolution of the Mn K pre-edge is not lost on charging.[20] Unfortunately, no simple direct analysis method to derive changes in local atomic arrangements and oxidation states of Mn ions[21] from the pre-edge spectra is presently available. Further theoretical development in simulating the Mn pre-edge for this class of materials is required. In this work, primary attention is given instead to the Mn K-edge EXAFS analysis of the first-shell coordination number, which is directly related to the local environment of the absorbing ion.

Figure 3 shows the Fourier-transformed Mn K-edge EXAFS spectrum. The most relevant change on delithiation is a systematic decrease in the first-shell Mn-O correlations at ~1.5 Å (uncorrected for the emitted photoelectron wave phase shift) that, like the pre-edge peaks, do not fully recover after discharge for Li and Mn rich layered oxides materials.[22] Similar remarks apply to the shoulder at ~3 Å, associated with the second nearest-neighbor oxygen atoms.

Although the first shell metal-oxygen coordination numbers of pure $LiMO_2$ and Li_2MnO_3 are in principle unambiguous (CN=6 expected for octahedral coordination), disorder in the real LMNO materialcomplicates the analysis. Atomic position disorder is accounted for in the EXAFS analysis by an effective Debye-Waller-like parameter σ^2, which reflects the variation in bond distances within a single scattering shell. Different bond lengths contribute to the EXAFS with slightly different frequencies and dampen the amplitude of a given shell. In addition, the number of atoms

within the scattering shell is also directly related to the EXAFS amplitude.[23] Therefore, the refined σ^2 and CN values are directly correlated. However, because the disorder parameter σ^2 has a k-weight dependence and CN does not, and the first shell Mn-O is mostly separated from higher scattering shells, the correlation between σ^2 and CN can be potentially minimized.[22, 24]

The analysis is performed by fitting CN for an assumed value of σ^2, with different k-weighting (k = 1, 2, 3) exponents. The resultant three curves intersect at the optimal, uncorrelated values of CN and σ^2.[22] Alternatively, since the LMNO data was taken in-situ on the same electrode during the charge cycle, a systematic, chronological analysis of all scans can be done to reveal the trend in the first-shell Mn-O coordination [cf. Fig 4]. This is accomplished by considering the Mn-O coordination to be octahedral, with CN=6, for the freshly prepared electrode. Subsequent scans are simultaneously fit with the constraint that the first-shell Mn-O coordination can either remain at 6 or decrease. Systematic errors for the in-situ experiment are expected to be similar from scan to scan. Accordingly, whereas absolute values derived for CN have some ambiguity, one has confidence in the resultant trend derived from in-situ, chronological analysis [cf. Fig. 4]. We specifically note that the consistency in the results for analyses perfomed with two vastly different strategies, shown in Figures 4 and 5, serves as an independent verification of the results.

The trend in the first-shell Mn-O CN for the in-situ LMNO electrode is shown in Fig. 4. After charging for ~18 hours the Mn-O CN begins to rapidly decrease from its initial value of 6. This point in the charge corresponds to ~230 mAh/g, or roughly ~80 mAh/g into the activation/plateau region of the first cycle.[12] 80 mAh/g represents approximately half of the total capacity in the activation plateau. With further charging, the Mn-O CN diminishes from 6 to to ~5.4 (±0.1) at the top of charge. Figures 5(a)-(b) show the complete CN vs. σ^2 analysis at various times along the first cycle charge for the data shown in Fig. 4. Figure 5(a) corresponds to the 2-18 hour portion of the charge where the Mn-O CN remains flat. The k-dependent series of fits reveals that while CN remains constant along the charge curve, prior to and part way into (~80 mAh/g) the activation plateau, there is a significant increase in the EXAFS disorder parameter (σ^2). During the subsequent time on test, between hours 20-24, σ^2 stabilizes somewhat and the Mn-O CN steeply declines. These data show, unambiguously, a trend of Mn-O undercoordination that increases as the first-cycle charge progresses along the activation plateau. Interestingly, the Ni oxygen CN is stable until close to the top of charge where a slight undercoordination is observed. The origin of the small change in metal-O correlations will be discussed in a subsequent section.

As discussed below, EXAFS cannot reveal whether the undercoordinated Mn arises from the actual loss of oxygen from the first-shell ligand environment, or, a change in coordination due to migration of Mn into a different coordination environment. These possibilities are discussed in section IV below.

III. Simulation

Simulations were performed to help characterize atomic rearrangements in Li and Mn rich layered oxides during the first charge. We employ first principles density functional theory in the PAW representation, as implemented in the VASP code,[25, 26]

Journal Name COMMUNICATION

at the GGA+U level of approximation, [27] using the PBE exchange correlation functional. [28]

Crystal Structure

Pristine Li_2MnO_3 adopts a monoclinic crystal structure, with symmetry C2/m. [29] The monoclinic distortion of Li_2MnO_3 is small, however, and the structure differs only minutely from that of the trigonal $R\bar{3}m$ space group adopted by numerous materials with composition $LiMO_2$. In the calculations performed in this work, supercells were constructed with cell vectors based on the $R\bar{3}m$ space group.

Atomic Arrangement in Simulation Cell

Previous simulations[30] suggested that ordering energies in lithium and manganese rich layered materials are high compared to thermal energies, which would favor decomposition into composite structures with Li_2MnO_3 and $LiMO_2$ phases. Experiment, however, has shown that domains do not grow appreciably beyond the nanoscale, which may indicate that the coarsening kinetics are sluggish. Some workers adhere to a solid-solution description of the Li and Mn rich layered oxide materials, while others refer to them as composites. Irrespective, short-range ordering at the nanoscale likely plays a key role in the overall behavior of lithium and manganese rich materials. [3]

In the present simulations a periodic array of striped ribbon-like domains oriented along a crystal axis parallel to the layers is assumed (Fig. 6). The $LiMO_2$ region is represented by a zigzag arrangement of Ni and Mn ions. [31] Predicted Li NMR spectra for the Li and Mn rich layered oxide with M=Co based on a superposition of striped domains are in reasonable agreement with experiment. [32] Although highly idealized, the structure in Fig. 6 appears to capture key features of the real material. We note that the incorporation of small regions with $LiMn_6$ ordering, as utilized herein, would be a requirement in both solid solution and nanocomposite descriptions.

Cell Size

We employ cells with n_z=8 sublayers (4O, 2LiMn$_2$, and 2Li layers). In-layer dimensions of (n_x, n_y) = (6,8) which correspond to 96 atom and 384 atom periodic cells. Most of the simulations were performed with only a single k-point, owing to the large cell size.

Cell Composition

Simulations were performed for a Li and Mn rich layered oxide with M=$Ni_{0.5}Mn_{0.5}$. The resultant composition is $Li_{7/6-x}Ni_{1/4}Mn_{7/12}O_2$, which differs slightly from the commonly synthesized composition $Li_{1.2}Mn_{0.6}Ni_{0.2}O_2$, as well as the LMNO composition $0.3Li_2MnO_3 \cdot 0.7LiMn_{0.5}Ni_{0.5}O_2$ (=$Li_{1.13}Mn_{0.57}Ni_{0.3}O_2$) on which in situ x-ray measurements were made. Domains in adjacent layers are stacked in the c-direction with minimal offset.

IV. Results and Discussion

A. Oxygen vacancies

a. Hole doping by delithiation

Delithiation of metal oxides introduces holes, either on proximate transition-metal-ion or oxygen-ion sites, or on a covalent combination of the two. In hole-doped late-transition-metal oxides of Cu, Ni, and Co, holes often reside primarily on the oxygen. [33, 34] In addition to this tendency for holes to reside on oxygen, oxidation of octahedrally coordinated tetravalent Mn to Mn^{5+} is known to be unfavorable from a crystal-field

perspective, [35] which further restricts the hole formation to oxygen ions during activation of Li and Mn rich layered oxides. Extension of the first charge of a Li and Mn rich layered oxide material into the plateau region at voltages above about 4.5 V (at which the $LiMO_2$ regions have already been almost fully delithiated), thus results, absent atomic rearrangement, in hole doping primarily on the oxygen sublattice. [36, 37]

In general, hole doping is familiar in various classes of metal oxides, e.g., the substituted NiO, $Li_xNi_{1-x}O$, [33] the layered compound $Li_{1-x}(NiMnCo)_{1/3}O_2$, [20] the superconducting cuprates, [38] etc.

Besides its effect on local electronic structure, hole doping raises the free energy of a system with respect to competing phases and structures, perhaps nudging it towards or across a phase boundary. The resultant destabilization may promote transformation to a different (electronic and/or atomic) structure, if kinetics permits. [39] Few general guidelines regarding these instabilities are known, however.

In the literature, hole-doped states are often characterized by the hole concentration p per transition metal ion, e.g., p(Ni)=x/(1-x) in $Li_xNi_{1-x}O$, $p(M)$=x in $Li_{1-x}(NiMnCo)_{1/3}O_2$ and p(Mn)=$2f$ in $Li_{2(1-f)}MnO_3$. It is reasonable to assume that destabilization of hole-doped metal oxides typically increases with (a) increasing $p(M)$, and (b) when the nominal oxidation state of the transition metal in the hole-doped system is relatively unfavorable, such as octahedral Mn^{5+}. Delithiation of $Li_{1-x}CoO_2$ beyond $p(M)$~0.5 is known to result in oxygen loss, and other transformations. [34] In $Li_{1-x}(NiMnCo)_{1/3}O_2$, the alloying with Mn and Ni appears to stabilize the structure, and enable a $p(M)$>0.5 with the original layered structure remaining essentially intact, although Co resists oxidation to the 4+ state. [20] In $Li_{2(1-f)}MnO_3 \cdot Li_yMO_2$, hole doping in the Li_2MnO_3 component (with y less than ~0.15) creates structural instabilities, as we discuss in detail in the remainder of this article. The results shown in Fig. 4 suggest that (bulk) instabilities occur for hole doping in $Li_{2(1-f)}MnO_3$ domains greater than p(Mn)≈0.5.

This result may appear to contradict the finding that voltage fade occurs at any level of activation, [2-4] i.e., any p(Mn) = $2f$ > 0. It is possible that the instabilities responsible for voltage fade at small f are related to transformations near the surface[40] rather than in the bulk, and that the critical value of p(Mn) near the surface is smaller than that in the bulk. Also, a thermodynamically unstable structure (at small f) may be stable in practice if transformation barriers are high. This issue remains to be resolved.

b. Refinements

EXAFS measurements along with simulations for (lithium rich) LMNO presented below suggest that the instability that results from hole doping manifests itself in a series of transformations that begin with the creation of oxygen vacancies on the 6c sublattice, and O-O bonds. This picture is consistent with results of Rietveld refinements of XRD spectra for Li and Mn rich layered oxides based on M=$Ni_{0.5}Mn_{0.5}$ which have shown partial depletion of the oxygen sublattice occupancy. [41, 42] Prior EXAFS analysis on an analogous material, $Li_{1.2}Cr_{0.4}Mn_{0.4}O_2$ [18] has revealed lowered Mn coordination after extensive delithiation, which likewise suggests displaced oxygen.

The essence of the transformation is that the oxygen ions displaced to create oxygen-sublattice vacancies pair with other oxygen ions (Evidence from dynamical simulation for oxygen-ion

COMMUNICATION

pairing is presented below). A vacancy concentration $c(V_O) = f/3$ on the oxygen sublattice within the Li_2MnO_3-like domains would compensate for a Li extraction fraction of f, so that the remaining lattice oxygen ions can maintain their nominal oxidation state of 2−. The diffraction measurements cited above [41, 42] appear to show oxygen vacancy concentrations of this order of magnitude at the top of charge. Removal of all the Li from the lithium layer in the simulation cells ($y=0$, $f=3/4$), for example, would correspond to an oxygen vacancy concentration $c_{max}(V_O)=0.25$ in the Li_2MnO_3 domains.

A threshold value of lithium extraction, f_{th}, may exist below which the oxygen sublattice remains intact, with few, or no oxygen vacancies created (cf. discussion near the end of section II). The existence of such a threshold is suggested by the delay of any significant coordination number deficit $\Delta CN(Mn) = 6-CN$ until a capacity ~230 mAh/g, well into activation, is reached (section II).

c. Simulation

The properties of oxygen vacancies in related systems have been the subject of previous static simulations, in which energy differences were calculated. Okamoto[43] treated O vacancies in pure Li_2MnO_3. Qian et al.[40] considered oxygen vacancies in the Ni-Mn Li excess material $Li_{7/6-x}Ni_{1/4}Mn_{7/12}O_2$, using a relatively small unit cell. (The atomic arrangement treated by Qian et al. might more closely represent solid-solution than domain behavior.) In both of these cases, oxygen vacancy formation energies were found to be inversely proportional to the delithiation fraction. Thus, the driving force to create oxygen vacancies increases with delithiation, or increasing $p(Mn)$. Okamoto found oxygen vacancy formation to be thermodynamically favorable at lithium extraction fraction $f_{th}=0.25$ for pure Li_2MnO_3, under the assumption that oxygen removed to form vacancies evolves as O_2 molecules.

We performed in this work first principles molecular dynamics for $Li_{7/6-x}Ni_{1/4}Mn_{7/12}O_2$ (or $Li_{2(1-f)}MnO_3 \bullet Li_yMO_2$). Molecular dynamics has the advantage of addressing, to an extent, both thermodynamic and kinetic properties. We select a pristine structure that incorporates the Li-Mn ordering of pure Li_2MnO_3, as well as a zigzag arrangement of Mn and Ni in the Li_yMO_2 regions. Domains in the form of stripes parallel to one of the hexagonal crystal axes are created (Fig. 6). A mixture of such striped arrangements was found to reproduce most of the features of the observed NMR spectra.[32]

The periodic unit cell contained 384 lattice sites. A static calculation was done for the pristine material ($y=1$; $f=0$), as a reference. The dynamical calculations (for $y=1$; $f \geq 0$), employed the same cell vectors as for the pristine material; the stresses that develop as a result of delithiation were found to be relatively small.

We consider several states of delithiation during the first charge activation: (1) $y=1$; $f=0$ (pristine state); (2) $y=0$; $f=0$ (threshold of activation plateau); (3) $y=0$; $f=3/8$ (half the Li-layer Li in the $Li_{2(1-f)}MnO_3$ domain region removed); (4) $y=0$; $f=3/4$ (all Li-layer Li in the domain region removed); (5) $y=0$; $f=1$ (all Li removed from $Li_{2(1-f)}MnO_3$ domains).

A three-step methodology is employed in the simulations for the lithium-deficient cells [$y=0$; $f \geq 0$]: (i) SD($t=0$), (ii) MD(t), (iii) SD(t). In step (i), the atomic coordinates are relaxed by steepest-descents (SD). In this step, some of the Li ions in the M layer migrate to the delithiated Li layer. In (ii), the cell evolves

dynamically by molecular dynamics simulation as a function of time, t, at temperature $T=1000$ K or 500 K. Very little relaxation occurs at 500 K, and therefore most of the simulations were performed at $T=1000$ K. The simulation was continued for a total time t_f of about 35 ps (with MD time intervals of 1 fs). In (iii), the resultant structure after dynamical evolution for time t_j (at several intervals $t_j \leq t_f$) was relaxed by steepest descents.

The majority of the MD simulations were done for case (4) [$y=0$, $f = ¾$], and $T=1000$ K, Fig. 7. With all of the Li-layer Li removed, the driving force for oxygen sublattice relaxation is strong. Several oxygen ions within the Li_2MnO_3 stripes are displaced to create oxygen-oxygen bonds. Each plotted point represents a property averaged over a 1 ps time interval. The red circles denoted the total number of O-O pairs with bond lengths below 1.7 Å.

At the outset, the number O-O pairs, $n(O_2)$ increases approximately linearly. If the oxygen-pair creation were a thermally activated process, such that

$$n(O_2) \sim N_O \nu t \ \exp(-\tfrac{\Delta E}{kT}) ,$$

where N_O is the number of oxygen ions in the Li_2MnO_3 stripes, and $\nu \approx 10^{13} s^{-1}$ is an attempt frequency, the barrier to displacement would be of order 0.5 eV. For a barrier of this magnitude, simulations at lower temperatures (e.g., 500 K) would not show significant oxygen-pair creation $n(O_2)$ on computationally accessible time scales. This is consistent with the results of our simulations at 500 K, which were conducted for a smaller total time interval t_f. Under Li-ion battery operating conditions, the characteristic times are of course much longer than those available in the simulation, and presumably enable oxygen displacement to occur at room temperature.

As mentioned, simulations were also performed at lesser levels of delithiation at $T=1000$K: case (2): [$y=0$, $f = 0$], and case (3) [$y=0$, $f = 3/8$]. No oxygen displacement was observed in either case for time intervals t_f of the order of several ps. This is consistent with the EXAFS measurement, which suggested that bulk instability occurs at $p(Mn) \approx 0.5$, as mentioned in section IV.A.a.

Most of the results presented below are for case (4) [$y=0$, $f = ¾$], $T=1000$ K, steps (i), (ii) and (iii).

B. Mn under-coordination

X-ray absorption spectra are sensitive to local environment, and can therefore help characterize changes in coordination. Mn K-edge EXAFS spectra have been analyzed to obtain Mn coordination numbers during the charge of LMNO, as described in section II. A simplified model of Mn coordination is presented here to illustrate some of the features. In the absence of Mn migration (cf. section C), the Mn coordination number deficit $\Delta CN(Mn)$ is related to the concentration of oxygen vacancies in the domains:

$$\Delta CN(Mn) = 6 - CN(Mn)$$
$$= c(V_O) \, [c(O)/c(Mn)] \, NN(Mn;O) = 6 \, c(V_O), \quad (1)$$

where $c(O)/c(Mn)=3$ is the ratio of oxygen to manganese ions in Li_2MnO_3 and $NN(Mn;O)=2$ is the number of Mn nearest

neighbors of an O ion in Li_2MnO_3. It is the Mn ions in the $Li_{2(1-f)}MnO_3$ domains (rather than in the $Li_yNi_{0.5}Mn_{0.5}O_2$ regions) of $xLi_2MnO_3 \cdot (1-x)LiNi_{0.5}Mn_{0.5}O_2$ that are expected to experience the greatest change in their environment after activation. Assuming ideal phase separation, the fraction of Mn ions located in Li_2MnO_3 domains is $f_{dom}(Mn) = 2x/[1+x]$, and the average change in coordination number is therefore, in this approximation

$$\Delta CN(Mn) = 6 f_{dom}(Mn) \, c(V_O) = (12x/[1+x]) \, c(V_O). \quad (2)$$

The molecular dynamics simulations, however, show that the assumptions underlying Eqs.(1) and (2) are oversimplified: (i) Mn ions can migrate to the Li layer, and (ii) interstitial oxygen ions displaced to form oxygen vacancies can coordinate with Mn ions in their displaced locations. These features are addressed in the following section.

C. Mn migration

The migration of transition element ions to the lithium layer during delithiation in the layered systems $LiMO_2$ and $Li_2M'O_3$ presents an obstacle to the design of materials that cycle without irreversible structural transformation. Some elements, such as Ga and Cr,[44, 45] tend to migrate even in the absence of oxygen vacancies, with only minimal delithiation. Trivalent Mn in $Li_{1-x}MnO_2$ has a tendency to migrate to the lithium layer, assisted by disproportionation.[8] On the other hand, tetravalent Mn, located in Li_2MnO_3 domains in pristine $xLi_2MnO_3 \cdot (1-x)LiMO_2$ appears stable in its octahedral site, even in the presence of delithiation, according to simulations presented below, as long as the oxygen sublattice remains intact, with few oxygen vacancies.

If Mn migration during activation does occur, it is desirable to establish its trigger. Simulations[23] have been performed of (TM layer) octahedral to (Li layer) octahedral migration of Mn in fully delithiated pure Li_2MnO_3, by traversal of an octahedral edge rather than an octahedral face, in the absence of oxygen vacancies. The work by Lee and Persson nominally addresses pure Li_2MnO_3.

Experiment suggests, however, that the first-charge instabilities in pure manganite differ significantly from those in the Li- and Mn-rich layered oxide materials, which contain nanoscale Li_2MnO_3 domains.[22] Furthermore, oxygen vacancy creation in the Li_2MnO_3 domains during activation seems likely, based on the above-mentioned refinements.[41, 42]

We do not observe octahedral-to-octahedral Mn migration in the MD simulation. Fig. 7 plots results for oxygen-pair creation and Mn migration vs. MD simulation time. No migration of Mn occurs before about 5 ps, when the oxygen sublattice is still intact. For $t > \approx 5$ ps, however, a sufficient number of oxygen vacancies (proportional to $n(O_2)$) had been created to facilitate the migration of Mn ions.

Static simulations have also suggested that oxygen vacancies facilitate Mn migration. Simulations for M=$Ni_{0.5}Mn_{0.5}$ ($Li_{7/6-x}Ni_{1/4}Mn_{7/12}O_2$) have recently appeared,[40] which show that oxygen vacancies in the Mn coordination shell make migration energetically more favorable. In work not presented in detail here, we have performed static simulations on a cell of composition $Li_{7/6-x}Ni_{1/4}Mn_{7/12}O_2$, with the striped structure used in our dynamical simulations described above. We find

qualitatively similar results to those of.[40] Cells with a minimal number of vacancies were considered: a Li trivacancy in the Li layer, to create a vacant tetrahedral site, and zero, one, or two oxygen vacancies coordinated to a Mn ion located close to the tetrahedral site. We find in these static calculations that the thermodynamic driving force for Mn migration is negative for a Mn ion with fewer than two oxygen vacancies in its coordination shell.

EXAFS provides an experimental test of the coordination numbers predicted by simulation. The dynamical simulations presented here for $Li_{1/6}Ni_{1/4}Mn_{7/12}O_2$ enable prediction of the coordination number deficits $\Delta CN(Mn)$ and $\Delta CN(Ni)$ at the top of the first charge, which can be compared with coordination numbers obtained from the analysis of EXAFS measurements described in section II. Fig. 8 shows the results of the simulation of $\Delta CN(Mn)$ and $\Delta CN(Ni)$ as a function of time. It was assumed in the analysis of the simulations that the first shell coordination of Mn (or Ni) includes all oxygen ions within a cutoff radius of 2.3 Å. We find simulated coordination deficits converge after times of tens of picoseconds to values $\Delta CN(Mn)|_{simul} \approx 0.4$, and $\Delta CN(Ni)|_{simul} \approx 0.2$.

Analysis of the in situ measurements on $Li_{1.13}Mn_{0.57}Ni_{0.3}O_2$ described in section II yielded a coordination deficit $\Delta CN(Mn)|_{expt} = 0.6 \pm 0.1$ and $\Delta CN(Ni)|_{expt} = 0.2 \pm 0.1$ at the top of charge, in close agreement with the simulated values given above. The level of agreement between theory and experiment increases one's confidence that the theoretical model captures significant features of the real material.

D. Oxygen interstitials

To create oxygen vacancies, lattice oxygen ions are displaced into interstitial sites. Although experimental evidence exists for the oxygen vacancies (cf. section A), the oxygen interstitials are more difficult to observe experimentally. Since only a fraction of the expected oxygen evolution/loss (that would be expected if one oxygen were lost per two lithium ions extracted) has actually been observed,[46-48] it seems reasonable to assume that a large fraction of any displaced oxygen remains in the material. The simulations are performed under the assumption that no oxygen is lost, so that there is a corresponding oxygen interstitial for each oxygen vacancy, i.e., $n(O_I) = n(V_O)$.

We analyzed the dynamical simulations to determine the total number of oxygen interstitials, $n(O_I)$, which are defined, operationally, as oxygen ions that lack a Mn (or Ni) ion neighbor within a bond length maximum of 2.3 Å. With this definition, we find that $n(O_I) \approx n(O_2)$. To obtain concentrations (rather than absolute numbers in the simulation cell) of these properties, we divide by the number of oxygen lattice sites in the Li_2MnO_3 stripes, $c(O_I) = n(O_I)/n(O) \approx n(V_O)/n(O)$. The simulated vacancy (or interstitial) concentration converges (after tens of picoseconds) to $c(V_O) \approx 0.25$. We pointed out in section A that for a model in which all displaced oxygen evolves (in response to full delithiation of the Li layers), the vacancy concentration $c_{max}(V_O) = 0.25$. Thus, although the oxygen in our model remains within the material rather than evolving, the oxygen vacancy concentration $c(V_O) \approx c_{max}(V_O)$. Incidentally, we find in MD simulations that when all of the lithium from the cell is removed, which results in a composition $Ni_{1/4}Mn_{7/12}O_2$, additional oxygen vacancies are created (case 5: y=0; f=1), in proportion to the increased level of hole doping, $p(Mn)$.

All of the $n(O_I)$ oxygen interstitials are bonded to (at least) one other oxygen ion, with and O-O bond length less than 1.7 Å. The smallest oxygen ion pair bond lengths are approximately 1.3 Å, which is close to the standard bond length for superoxide. The ions within such pairs are relatively distant (isolated) from metal ions in the cell. The number of isolated pairs is of order 40% of $n(O_2)$. At least one member of oxygen ion pairs with larger bond lengths (e.g., in the peroxide range, 1.5 Å) interacts with other ions in its vicinity.

An experimental signature of interstitial oxygen bound in molecules or clusters would be extremely valuable. XPS has been suggested as such a probe[49-51] although it is limited to the near surface region. It would be of interest to confirm that oxygen molecules with different charge states (superoxide and peroxide) occur after activation. The presence of a spectrum of O-O bond lengths (between 1.3 and 1.7 Å) makes the identification of oxygen molecules particularly challenging.

An important question is whether the oxygen complexes are mobile. Lu and Dahn[41] estimated that a diffusion coefficient of about 10^{-13} cm^2/s would be required for the interstitial oxygen to escape primary particles of size 200 nm. The corresponding effective migration energy would be roughly 0.5 eV or below. Our simulations suggest that most of the oxygen interstitials are bound in complexes with higher migration barriers. Therefore, we believe that most of the oxygen interstitials do not migrate far from the vacancies from which they are created.

E. Evolution of structure during first charge

The simulations presented in this work suggest a sequence of transformations that Li and Mn rich layered oxide materials undergo during the first charge. In this section, we summarize these transformations, some of which have been discussed above.

Simulations for pure Li_2MnO_3 [52] with a small concentration of Li vacancies yielded Li migration barriers of order 0.6 eV for both intra- and inter-layer migration paths, small enough for migration to occur at room temperature. In the present simulations of LMNO, with full Li-layer delithiation, we find migration of the $LiMn_2$-layer Li occurs spontaneously, without thermal activation. This is illustrated in the lower panel of Fig. 9, which shows the atomic configuration after a steepest descents relaxation of $Li_{7/6-x}Ni_{1/4}Mn_{7/12}O_2$ (with $x=1$, i.e., all Li-layer lithium removed). Li ions are denoted by green spheres in Fig. 8. Some Li ions initially located in the $LiMn_2$-layer have migrated to the delithiated Li layer.

In the dynamical simulation, oxygen ions are the first ions heavier than Li to migrate (Fig. 7), driven by their weakened M-O bonding in the delithiated state, as discussed above. The disruption of the oxygen sublattice enables the Mn to migrate across an oxygen layer into a Li layer (after about $t=5$ ps; cf. Fig. 7). By tracking the path of the first Mn ions to migrate, we verify that these ions initially occupy tetrahedral sites, which are metastable. As more and more oxygen ion vacancies are created, the lattice structure becomes increasingly disordered, as the oxygen vacancy concentration approaches $c(V_O) \approx 0.25$. For such high vacancy concentrations, the oxygen sublattice in the domain region is not maintained, and the (octahedral or tetrahedral) symmetry of its interstices is lost. Thus, it is difficult to identify the sites that Mn has migrated to in the Li layer as either octahedral or tetrahedral, in the top panel of Fig. 9, although some of the migrated Mn ions do adopt four- and five-fold

coordination, while others retain six-fold coordination. It is conceivable that such under-coordinated Mn ions may contribute to enhanced intensity that appears in the Mn pre-edge region discussed in connection with Fig. 2. In the top panel, we see that most of the Li ions have migrated to the $LiMO_2$ region (left side of figure).

The coordination numbers for Ni ions plotted in Fig. 8 show that the first charge alters the local environment of Ni as well as Mn. The Ni ions essentially remain in the same sites as in the pristine material, but some of the coordinated oxygen has migrated, which lowers CN(Ni). CN(Ni) converges later in the MD simulation than CN(Mn). Ni ions in the vicinity of the interfaces between Li_2MnO_3 and $LiMO_2$ stripes are the ones most affected by the transformations during the first charge. Mn ion environments throughout the stripe are affected during the first charge. Approximately 1/3 of the Mn ions move across an adjacent oxygen layer into what was the Li layer in the pristine material.

The crystalline order of the $LiMO_2$ component remains intact. Therefore, despite the severely disordered structure of the delithiated Li_2MnO_3 stripes, the XRD spectra for this model structure remains crystalline. Thus XRD simulations (not presented here) show that the most prominent peaks found for the assumed pristine structure persist in the structure after MD simulation of the first charge.

As noted above, the oxygen ions displaced in the Li_2MnO_3 stripes bond with other oxygen ions to form oxygen-molecule-like entities (Fig. 9). The oxygen ions in shorter bond length molecules (bond length about 1.3 Å) are denoted by the gray spheres, and those belonging to longer bond length molecules by greenish-brown spheres; oxygen ions bonded exclusively to metal ions are denoted by red spheres.

The transformations outlined in this section are driven by the large energy lowering that is achieved by rebonding a fraction of oxygen ions as oxygen molecules or clusters. The oxygen displacement (which contributes to $n(O_I)$) and rebonding (which contributes to $n(O_2)$) proceeds until there are approximately two oxygen ions per Mn ion in the Li_2MnO_3 region that are primarily bonded to Mn: $MnO_3 \rightarrow MnO_2 + 1/2 O_2$ (in the case of full delithiation). The simulation indicates that the energy lowering between the structures represented in the two panels of Fig. 9 is about 300 meV per $Li_{1/6}Ni_{1/4}Mn_{7/12}O_2$ formula unit, or about 1 eV per interstitial oxygen.

V. Discussion

We have addressed the transformations that occur during the first charge of $x Li_2MnO_3 \bullet (1-x)LiMO_2$, where $M=Ni_{0.5}Mn_{0.5}$. Hole doping during first-charge activation creates a thermodynamic driving force for oxygen displacement and rearrangement that results in oxygen-oxygen bonding; the oxygen-ion rearrangement is, after an initial interval (5 ps at 1000 K), accompanied by Mn ion migration to the Li layer. Dynamical simulations demonstrate these instabilities in a structure based on striped domains with an assumed thickness and orientation. This is an idealization, and the real material likely contains a spectrum of stripe thicknesses, orientations, inter-layer offsets, etc. For a given chemical composition, however, the thermodynamic driving force for atomic rearrangements during activation would persist regardless of the details of the pristine structure, although kinetics may differ for different pristine material structures.

The validity of the simulations presented here depends on whether the dynamical evolution of the structure at 1000 K for tens of picoseconds is representative of that of the real system at room temperature over laboratory time scales. Such an equivalence certainly cannot be taken for granted for all chemical compositions, however, it is at least plausible that the results for M=Ni$_{0.5}$Mn$_{0.5}$ are representative for most members of the class of Li and Mn rich layered oxides xLi$_2$MnO$_3$•(1-x)LiMO$_2$.

VI. Conclusions

EXAFS experiments in combination with first principles simulation suggest that oxygen vacancies and O-O bonds are created during the first charge of LMNO. Simulations indicate that oxygen vacancies destabilize Mn in the LiMn$_2$ layers of domains, and enable a fraction of the Mn (as well as Li) to migrate to the Li layer.

The simulations indicate that oxygen interstitials, a by-product of the oxygen vacancies, are paired with other oxygen ions with a bond length of 1.3 - 1.7 Å. The resultant homopolar bonding compensates for the degraded metal-oxygen bonding in the electron-deficient delithiated material.

REFERENCES

1. M. M. Thackeray, S.-H. Kang, C. S. Johnson, J. T. Vaughey, R. Benedek and S. A. Hackney, *Journal of Materials Chemistry*, 2007, 17, 3112-3125.

2. J. R. Croy, D. Kim, M. Balasubramanian, K. Gallagher, S. H. Kang and M. M. Thackeray, *Journal of the Electrochemical Society*, 2012, 159, A781-A790.

3. J. R. Croy, K. G. Gallagher, M. Balasubramanian, B. R. Long and M. M. Thackeray, *Journal of The Electrochemical Society*, 2014, 161, A318-A325.

4. M. Bettge, Y. Li, K. Gallagher, Y. Zhu, Q. L. Wu, W. Q. Lu, I. Bloom and D. P. Abraham, *Journal of the Electrochemical Society*, 2013, 160, A2046-A2055.

5. D. Mohanty, A. S. Sefat, J. L. Li, R. A. Meisner, A. J. Rondinone, E. A. Payzant, D. P. Abraham, D. L. Wood and C. Daniel, *Physical Chemistry Chemical Physics*, 2013, 15, 19496-19509.

6. D. Mohanty, J. Li, D. P. Abraham, A. Huq, E. A. Payzant, D. L. Wood and C. Daniel, *Chemistry of Materials*, 2014, 26, 6272-6280.

7. Y. Kan, Y. Hu, C.-K. Lin, Y. Ren, Y.-K. Sun, K. Amine and Z. Chen, *Physical Chemistry Chemical Physics*, 2014, 16, 20697-20702.

8. J. Reed, G. Ceder and A. Van Der Ven *Electrochemical and Solid-State Letters*, 2001, 4, A78-A81.

9. K. G. Gallagher, J. R. Croy, M. Balasubramanian, M. Bettge, D. P. Abraham, A. K. Burrell and M. M. Thackeray, *Electrochemistry Communications*, 2013, 33, 96-98.

10. J. R. Croy, K. G. Gallagher, M. Balasubramanian, Z. Chen, Y. Ren, D. Kim, S.-H. Kang, D. W. Dees and M. M. Thackeray, *The Journal of Physical Chemistry C*, 2013, 117, 6525-6536.

11. F. Dogan, B. R. Long, J. R. Croy, K. G. Gallagher, H. Iddir, J. T. Russell, M. Balasubramanian and B. Key, *Journal of the American Chemical Society*, 2015, 137, 2328-2335.

12. C. S. Johnson, J. S. Kim, C. Lefief, N. Li, J. T. Vaughey and M. M. Thackeray, *Electrochemistry Communications*, 2004, 6, 1085-1091.

13. S. Kraft, J. Stümpel, P. Becker and U. Kuetgens, *Review of Scientific Instruments*, 1996, 67, 681-687.

14. B. Ravel and M. Newville, *Journal of Synchrotron Radiation*, 2005, 12, 537-541.

15. B. Ravel and M. Newville, *Physica Scripta*, 2005, 2005, 1007.

16. Z. Lu, D. D. MacNeil and J. R. Dahn, *Electrochemical and Solid-State Letters*, 2001, 4, A191-A194.

17. M. Oishi, T. Fujimoto, Y. Takanashi, Y. Orikasa, A. Kawamura, T. Ina, H. Yamashige, D. Takamatsu, K. Sato, H. Murayama, H. Tanida, H. Arai, H. Ishii, C. Yogi, I. Watanabe, T. Ohta, A. Mineshige, Y. Uchimoto and Z. Ogumi, *Journal of Power Sources*, 2013, 222, 45-51.

18. M. Balasubramanian, J. McBreen, I. J. Davidson, P. S. Whitfield and I. Kargina *Journal of The Electrochemical Society*, 2002, 149, A176-A184.

19. N. Yabuuchi, K. Yoshii, S.-T. Myung, I. Nakai and S. Komaba, *Journal of the American Chemical Society*, 2011, 133, 4404-4419.

20. W.-S. Yoon, M. Balasubramanian, K. Y. Chung, X.-Q. Yang, J. McBreen, C. P. Grey and D. A. Fischer, *Journal of the American Chemical Society*, 2005, 127, 17479-17487.

21. F. Farges, *Physical Review B*, 2005, 71, 155109.

22. J. R. Croy, J. S. Park, F. Dogan, C. S. Johnson, B. Key and M. Balasubramanian, *Chemistry of Materials*, 2014, 26, 7091-7098.

23. E. Lee and K. A. Persson, *Advanced Energy Materials*, 2014, 4, 1400498.

24. B. Ravel, http://cars9.uchicago.edu/~ravel/course/notes.html, 2000.
25. G. Kresse and J. Furthmüller, *Physical Review B*, 1996, 54, 11169.
26. G. Kresse and D. Joubert, *Physical Review B*, 1999, 59, 1758-1775.
27. S. L. Dudarev, G. A. Botton, S. Y. Savrasov, C. J. Humphreys and A. P. Sutton, *Phys. Rev. B*, 1998, 57, 1505-1509.
28. J. P. Perdew, K. Burke and M. Ernzerhof, *Physical Review Letters*, 1996, 77, 3865.
29. P. Strobel and B. Lambert-Andron, *Journal of Solid State Chemistry*, 1988, 75, 90-98.
30. H. Iddir and R. Benedek, *Chemistry of Materials*, 2014, 26, 2407-2413.
31. J. Breger, K. Kang, J. Cabana, G. Ceder and C. P. Grey, *Journal of Materials Chemistry*, 2007, 17, 3167-3174.
32. H. Iddir, B. Key, F. Dogan, J. T. Russell, B. R. Long, J. Bareno, J. R. Croy and R. Benedek, *Journal of Materials Chemistry A*, 2015, 3, 11471-11477.
33. P. Kuiper, G. Kruizinga, J. Ghijsen, G. A. Sawatzky and H. Verweij, *Physical Review Letters*, 1989, 62, 221.
34. A. Van der Ven, M. K. Aydinol, G. Ceder, G. Kresse and J. Hafner, *Physical Review B*, 1998, 58, 2975-2987.
35. J. A. Saint, M. M. Doeff and J. Reed, *Journal of Power Sources*, 2007, 172, 189-197.
36. H. Koga, L. Croguennec, M. Ménétrier, K. Douhil, S. Belin, L. Bourgeois, E. Suard, F. Weill and C. Delmas, *Journal of The Electrochemical Society*, 2013, 160, A786-A792.
37. R. Xiao, H. Li and L. Chen, *Chemistry of Materials*, 2012, 24, 4242-4251.
38. Y. J. Chen, M. G. Jiang, C. W. Luo, J. Y. Lin, K. H. Wu, J. M. Lee, J. M. Chen, Y. K. Kuo, J. Y. Juang and C.-Y. Mou, *Physical Review B*, 2013, 88, 134525.
39. R. Hausbrand, G. Cherkashinin, H. Ehrenberg, M. Gröting, K. Albe, C. Hess and W. Jaegermann, *Materials Science and Engineering: B*, 2015, 192, 3-25.
40. D. Qian, B. Xu, M. Chi and Y. S. Meng, *Physical Chemistry Chemical Physics*, 2014, 16, 14665-14668.
41. Z. Lu and J. R. Dahn, *Journal of the Electrochemical Society*, 2002, 149, A815-A822.
42. C. R. Fell, D. Qian, K. J. Carroll, M. Chi, J. L. Jones and Y. S. Meng, *Chemistry of Materials*, 2013, 25, 1621-1629.
43. Y. Okamoto, *Journal of the Electrochemical Society*, 2011, 159, A152-A157.
44. N. K. Karan, D. P. Abraham, M. Balasubramanian, M. M. Furczon, R. Thomas and R. S. Katiyar, *Journal of The Electrochemical Society*, 2009, 156, A553-A562.
45. M. Balasubramanian, J. McBreen, K. Pandya and K. Amine, *Journal of The Electrochemical Society*, 2002, 149, A1246-A1249.
46. A. R. Armstrong, M. Holzapfel, P. Nova¡k, C. S. Johnson, S.-H. Kang, M. M. Thackeray and P. G. Bruce, *Journal of the American Chemical Society*, 2006, 128, 8694-8698.
47. N. Tran, L. Croguennec, M. Ménétrier, F. Weill, P. Biensan, C. Jordy and C. Delmas, *Chemistry of Materials*, 2008, 20, 4815-4825.
48. F. La Mantia, F. Rosciano, N. Tran and P. Novák, *Journal of The Electrochemical Society*, 2009, 156, A823-A827.
49. K. Nakahara, M. Tabuchi, S. Kuroshima, A. Toda, K. Tanimoto and K. Nakano, *Journal of The Electrochemical Society*, 2012, 159, A1398-A1404.
50. M. Sathiya, G. Rousse, K. Ramesha, C. P. Laisa, H. Vezin, M. T. Sougrati, M. L. Doublet, D. Foix, D. Gonbeau, W. Walker, A. S. Prakash, M. Ben Hassine, L. Dupont and J. M. Tarascon, *Nat Mater*, 2013, 12, 827-835.
51. M. Sathiya, A. M. Abakumov, D. Foix, G. Rousse, K. Ramesha, M. Saubanère, M. L. Doublet, H. Vezin, C. P. Laisa, A. S. Prakash, D. Gonbeau, G. VanTendeloo and J. M. Tarascon, *Nat Mater*, 2015, 14, 230-238.
52. C. Yong-Chang, H. Miao, L. Yang, C. Tong, L. Cheng-Cai, L. Qiang, S. Zhao-Lin and S. Li-Juan, *Chinese Physics Letters*, 2015, 32, 017102.
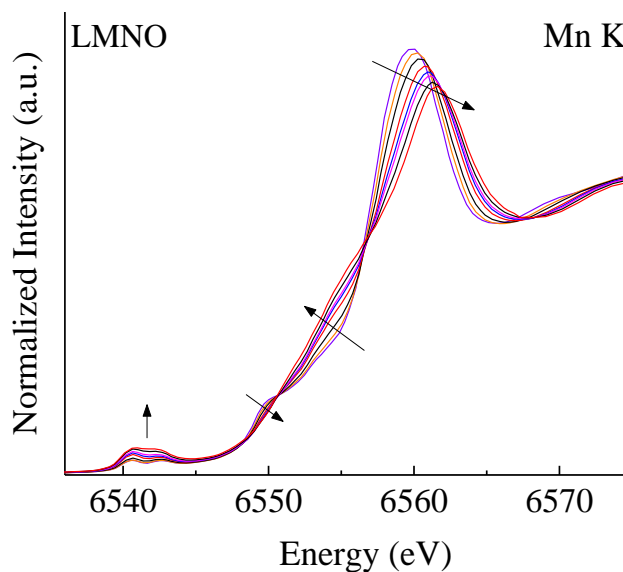

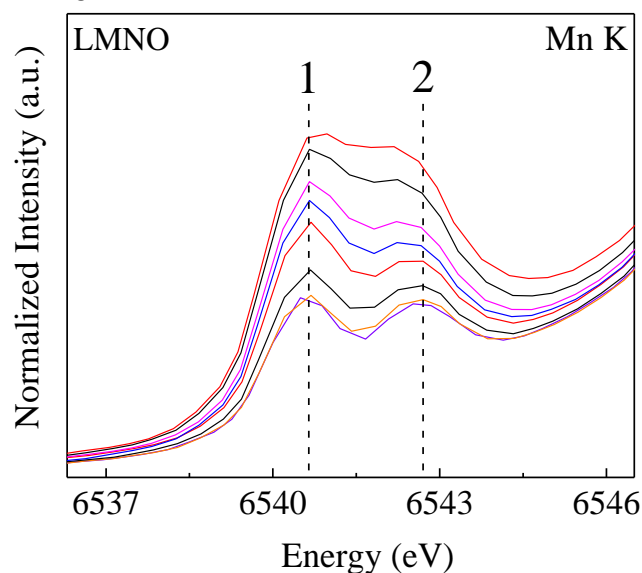Fig. 1. In situ XANES spectra for LMNO at intervals during first charge.

Fig. 2. Pre-edge regions of in situ Mn K-edge XANES spectra for LMNO at intervals during first charge.
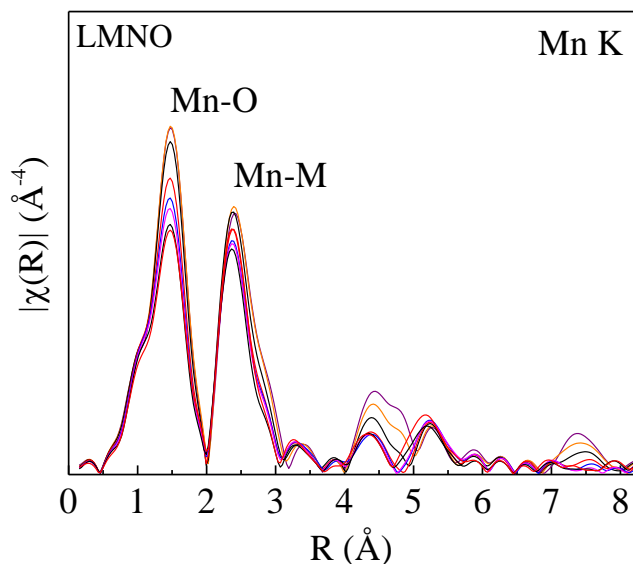
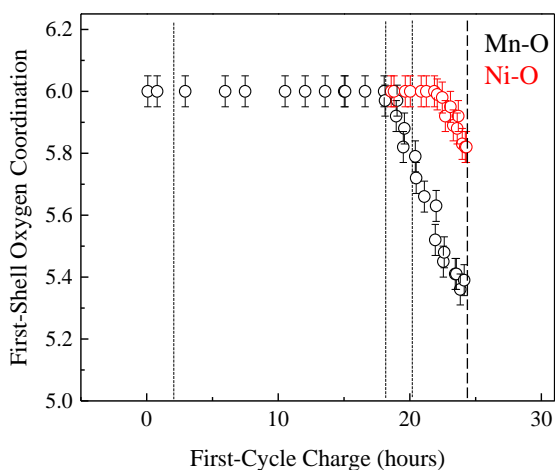Fig. 3 Fourier transform of EXAFS spectra in Fig. 2.

Fig. 4. Coordination number (CN) of Mn and Ni during first charge of LMNO. The vertical dashed lines can be used as a guide to compare to the coordination of Mn determined in figure (5). Notably, the correspondence in the value for CN extracted by the two independent methods is excellent.
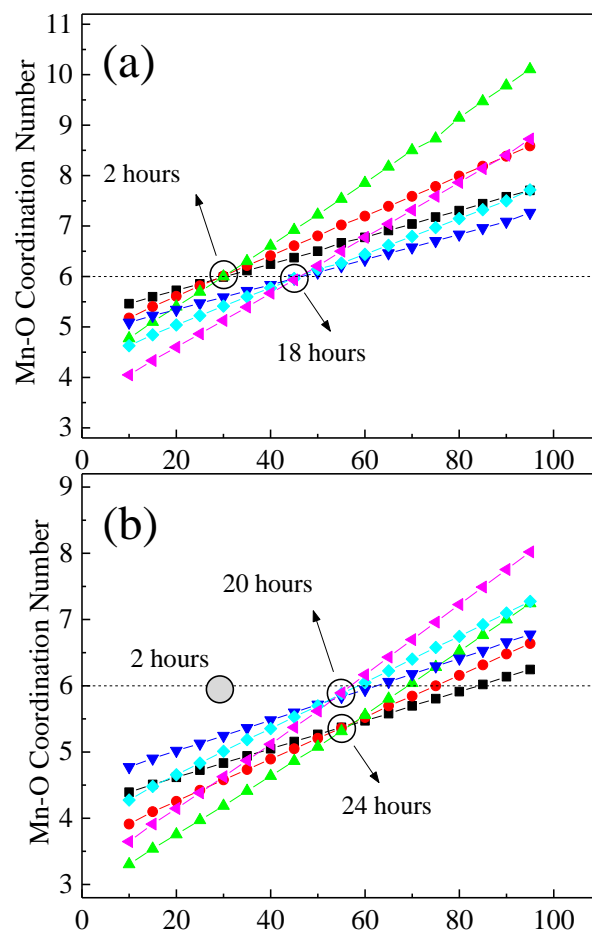

Fig. 5. k-weight (k=1, 2, 3) dependent fits of the first-shell, Mn-O CN and σ^2 along the first-cycle charge for LMNO. Each series is marked by the time of the scan as shown in Fig. 4. Circles show the point of intersection and dashed lines mark the nominal CN of the fresh material, CN=6. The shaded circle in b) reproduces the 2-hour intersection shown in a) for comparison.
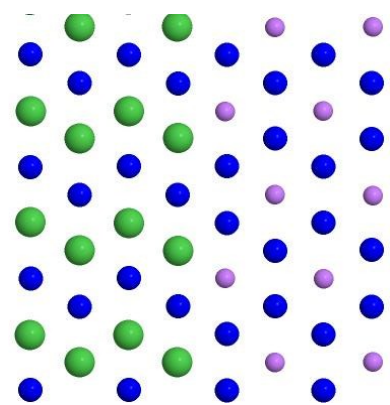

Fig. 6. Schematic illustration of ribbon domain in metal layer of xLi$_2$MnO$_3$•(1-x)LiMO$_2$ with (M=Ni$_{i0.5}$Mn$_{0.5}$). Li: purple; Mn: blue; Co: green.
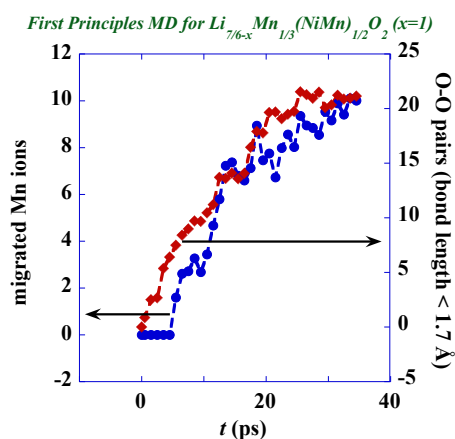
Fig. 7. Oxygen-oxygen bonds and migrated Mn ions as a function of simulation time, in ps, for LMNO cell with Li-layer Li removed. There are 32 Mn ions in the LiMn$_2$ stripes, so that $10/32 \approx 1/3$ of the domain Mn ions migrate across an oxygen layer. 48 Li ions are removed from the domains, and therefore approximately one O-O pair is formed for every two Li ions removed.
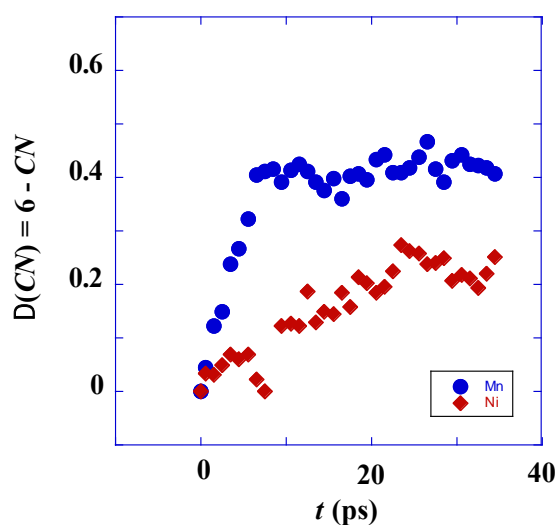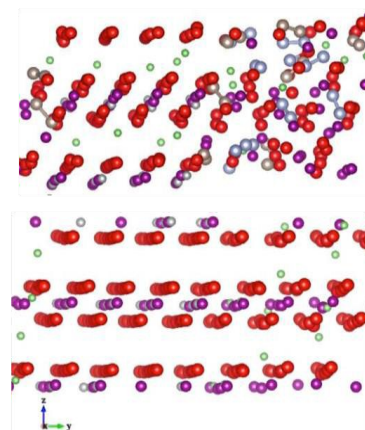

Fig. 9. Atomic structure of Li$_{1/6}$Ni$_{1/4}$Mn$_{7/12}$O$_2$ before dynamical simulation (lower panel), and after dynamical simulation at 1000 K for 35 ps (upper panel). The domain stripes run perpendicular to the plane of projection. The left side of each panel represents the LiMO$_2$ region, and the right side the Li$_2$MnO$_3$. In the dynamical simulation, about ¼ of the oxygen ions in the domains (right-hand side) are displaced from their lattice sites and rebond with other oxygen. The oxygen lattice in the LiMO$_2$ region maintains its crystallinity however, and the overall structure exhibits diffraction peaks. Li: green; Ni: grey; Mn: purple; oxygen red; displaced oxygen that forms "free" molecules: blue; displaced oxygen pairs that maintain bonds with Mn: brown.

Fig. 8. Simulated coordination number deficit for Mn and Ni in Li$_{1/6}$Ni$_{1/4}$Mn$_{7/12}$O$_2$ as a function of time.